PCCP

PAPER

View Article Online
View Journal | View Issue

Cite this: *Phys. Chem. Chem. Phys.*, 2015, **17**, 3072

The role of oxygen vacancies and their location in the magnetic properties of $Ce_{1-x}Cu_xO_{2-\delta}$ nanorods

M. I. B. Bernardi,[a] A. Mesquita,[b] F. Béron,[c] K. R. Pirota,[c] A. O. de Zevallos,[d] A. C. Doriguetto[d] and H. B. de Carvalho*[d]

Received 25th October 2014,
Accepted 1st December 2014

DOI: 10.1039/c4cp04879b

www.rsc.org/pccp

Ceria (CeO_2) is a promising dilute magnetic semiconductor. Several studies report that the intrinsic and extrinsic structural defects are responsible for room temperature ferromagnetism in undoped and transition metal doped CeO_2 nanostructures; however, the nature of the kind of defect necessary to promote and stabilize the ferromagnetism in such a system is still a matter of debate. In the work presented here, nanorods from the system $Ce_{1-x}Cu_xO_{2-\delta}$ with x = 0, 0.01, 0.03, 0.05 and 0.10, with the more stable {111} surface exposed were synthesized by a microwave-assisted hydrothermal method. A very careful structure characterization confirms that the Cu in the samples assumes a majority 2+ oxidation state, occupying the Ce (Ce^{4+} and Ce^{3+}) sites with no secondary phases up to x = 0.05. The inclusion of the Cu^{2+} in the CeO_2 structure leads to the introduction of oxygen vacancies in a density proportional to the Cu^{2+} content. It is supposed that the spatial distribution of the oxygen vacancies follows the Cu^{2+} distribution by means of the formation of a defect complex consisting of Cu^{2+} ion and an oxygen vacancy. Superconducting quantum interference device magnetometry demonstrated a diamagnetic behavior for the undoped sample and a typical paramagnetic Curie–Weiss behavior with antiferromagnetic interactions between the Cu^{2+} ions for the single phase doped samples. We suggest that the presence of oxygen vacancies is not a sufficient condition to mediate ferromagnetism in the CeO_2 system, and only oxygen vacancies in the surface of nanostructures would lead to such a long range magnetic order.

1. Introduction

Ceria (CeO_2) nanostructures have attracted the interest of many researchers in the past decade due to their great potential for applications in catalysis, electrochromic devices, gas sensors, ultraviolet radiation detectors, environmentally-friendly pigments, gamma radiation dosimetry, *etc.*[1] Concerning its magnetic properties, room temperature ferromagnetism (RTFM) for transition metal doped[2] and undoped[3] systems have been observed in some experimental results. These results launch the CeO_2 systems to the class of materials known as dilute magnetic oxides (DMOs) with potential for application in the development of spintronic devices. Moreover, due to its cubic structure and cell parameter close to the Si, the CeO_2 systems also have the desirable advantage of easy integration to the conventional electronic devices.[4]

For DMOs the main theoretical models that take into account the observed RTFM for the different oxide matrices are the d^0 magnetism for undoped systems,[5] the bound magnetic polaron (BMP) theory,[6] and the carrier-mediated mechanism,[7] the latter two for the transition metal (TM) doped systems. It is important to also mention a sub-category of BMP theory named F-center exchange (FCE).[8] In all these models the defect concentration plays an important role. In the d^0 magnetism the defects by themselves are responsible for the RTFM by means of a spin polarized density of states around the Fermi level, whereas in the BMP theory the defects are responsible for the ferromagnetic coupling between the magnetic ions used to dope the oxide matrix, and in the carrier-mediated mechanism the free charge carriers introduced into the system by donor or acceptor-like defects are the ones responsible for the ferromagnetic coupling. In this context, the origin of the observed RTFM for doped and undoped oxides and its relation to a specific group of defects is still a matter of debate.[9–15]

Nanostructured CeO_2 samples are normally nonstoichiometric compounds of the type $CeO_{2-\delta}$ due the loss of oxygens at the surfaces of the nanoparticles to the surround environment.

[a] *Instituto de Física de São Carlos, USP – Universidade de São Paulo, 13560-970 São Carlos, SP, Brazil*
[b] *Departamento de Física, Instituto de Geociências e Ciências Exatas, Universidade Estadual Paulista, 13500-970 Rio Claro, SP, Brazil*
[c] *Instituto de Física Gleb Wataghin, Universidade Estadual de Campinas, 13083-859 Campinas, SP, Brazil*
[d] *Universidade Federal de Alfenas, 37130-000 Alfenas, MG, Brazil. E-mail: bonette@unifal-mg.edu.br*

As a consequence of the introduced oxygen vacancies (V_O), a reduction of the Ce^{4+} ions to Ce^{3+} occurs in these regions, leading to a lattice expansion for $CeO_{2-\delta}$ nanoparticles.[16,17] Sundaresan *et al.*[3] suggested that all metal oxides in the nanoparticulate form would exhibit room-temperature ferromagnetism due to the exchange interactions between unpaired electron spins arising from oxygen vacancies at the nanoparticle surface. After Sundaresan, a variety of experimental and theoretical papers reported the observation of RTFM in doped and undoped nanostructured CeO_2 samples and also correlated it with oxygen vacancies.[18–21] On the other hand, Liu *et al.*[22] showed that oxygen vacancies do not mediate the ferromagnetism in undoped CeO_2 nanostructures, but instead cerium vacancies would be the responsible for the observed RTFM. Fernandes *et al.*[9] observed a considerable decrease of the magnetization saturation with the storage time (age). These authors associated this behavior with an oxidation process (loss of oxygen vacancies) and concluded that part of observed ferromagnetic behavior could be directly associated with this kind of defect. However, after a long period of storage, a low effective remnant magnetization was observed and, like Liu *et al.*,[22] this fraction of the observed RTFM was attributed to Ce vacancies. All the last cited references[9,18–23] argue that the most important defects associated with the RTFM would be located at the surface of the grains or nanoparticles, following Sundaresan *et al.*[3]

In the present work, nanorods from the system $Ce_{1-x}Cu_xO_{2-\delta}$ with x = 0, 0.01, 0.03, 0.05 and 0.10, with the higher stable {111} surface exposed (growth direction [211]) were synthesized using a microwave-assisted hydrothermal method. This synthesis method combines the advantages of both hydrothermal and microwave-irradiation techniques such as very short reaction time, production of small particles with a narrow size distribution and high purity.[24] Nanostructured Cu-doped CeO_2 ($Ce_{1-x}Cu_xO_{2-\delta}$) materials are of considerable interest because of their high catalytic activity. Several reports in the literature have proved that the $Ce_{1-x}Cu_xO_{2-\delta}$ system is an efficient catalyst for the selective CO oxidation,[25] the hydrogen combustion reaction,[26] and for the water–gas shift (WGS) reaction,[27] just to cite few examples. In the context of the dilute magnetic semiconductors, the Cu doping has the advantage that the metallic dopant, as well as all possible dopant-based secondary phases, are nonferromagnetic.[28] Therefore, if any ferromagnetism is observed in a Cu-based system, it will undoubtedly be an intrinsic property of the material. Moreover, the most stable oxidation state of Cu is 2+;[29] for this reason, the introduction of Cu into the CeO_2 matrix in a substitutional character of the Ce ions (Ce^{4+} and Ce^{3+}) leads, by a charge-compensation process,[30] to the introduction of oxygen vacancies into the system in double the proportion of the Cu^{2+} concentration ($\delta = 2x$).[31] The doping of the CeO_2 matrix with nonferromagnetic elements was reported for different groups.[19,32] Here, the conclusions are also controversial; while most of them associated the ferromagnetic properties with oxygen vacancies, Chen *et al.*[32] attributed the observed ferromagnetism to lattice distortions caused by the smaller size of the dopant. In the special case of Cu doping there are few reports in the literature concerning its magnetic properties. Slusser *et al.*[33] reported paramagnetism (PM) in undoped and RTFM in Cu doped CeO_2. Seehra *et al.*[34] observed a small RTFM component superimposed in a main PM component for both undoped and Cu-doped CeO_2 nanoparticles, for the undoped CeO_2 samples the observed RTFM was attributed to Fe impurities. However, for Cu-doped samples they observed a correlation between the PM and the RTFM components and the Cu content and the observed magnetic properties were argued to be an intrinsic effect due to Cu doping. Based on the Slusser and Seehra reports, Li *et al.*[35] performed first-principles calculations within density-functional theory (DFT) to study the origin of the magnetism in Cu-doped CeO_2. In their report they concluded that the Cu doping by itself could not account for the observed RTFM. However, they found that a strong ferromagnetic coupling could be achieved between the defect complexes $Cu^{2+} + V_O$. In another article, Fernandes *et al.*[36] reported the loss of magnetization when the CeO_2 matrix was doped with transition metals. The observed magnetic behavior was analyzed under the scope of the F-center exchange (FCE) interaction model.[8] It was argued that the dopant elements change the spatial-charge density distribution impairing the formation of magnetic moments along the volume of the sample. In the context of the aforementioned research, the main goal of our work was to elucidate the ambiguous situation concerning the influence of oxygen vacancies and the Cu doping on the magnetic properties of nanostructured CeO_2 systems.

2. Experimental

In a typical procedure for obtaining $Ce_{1-x}Cu_xO_{2-\delta}$ (x = 0.01, 0.03, 0.05 and 0.10) nanostructures, 0.02 mol of the precursors, cerium chloride ($CeCl_3{\cdot}7H_2O$) and copper chloride ($CuCl_2{\cdot}2H_2O$), were dissolved in 50 mL of distilled water. Then, 50 mL of 10 mol L^{-1} NaOH was added rapidly under vigorous stirring. The mixed solution was placed in a 110 mL Teflon autoclave reaching 90% of its volume, which was sealed and placed in a microwave hydrothermal system, applying 2.45 GHz of microwave radiation at the maximum power of 800 W. The as-prepared solution was subjected to a microwave hydrothermal synthesis temperature of 140 °C for 10 min at a heating rate of 140 °C min^{-1} and then air-cooled at room temperature. The as-obtained precipitate powder was washed several times with distilled water and isopropyl alcohol and then dried at 60 °C for 24 h.

The powders were characterized structurally in an X-ray diffractometer (Rigaku, Rotaflex RU200B) with CuKα radiation (50 kV, 100 mA, λ = 1.5405 Å), using a θ–2θ configuration and a graphite monochromator. The scanning range was between 20 and 80° (2θ), with a step size of 0.02° and a step time of 5.0 s. A Rietveld analysis was performed using the program GSAS.[37] The size and morphology of the samples were determined by transmission electron microscopy (TEM) using a JEOL JEM 2010 URP, operating at 200 keV. Raman spectroscopy was carried out at room temperature in a Jobin-Yvon-64000 micro-Raman system in the backscattering geometry, using the 488 nm line of an Ar^+ laser for excitation. We used an optical lens with 100× magnification, which supplies an average laser spot size of 1 μm. X-ray absorption near edge spectroscopy (XANES) and extended X-ray absorption

fine structure (EXAFS) measurements at the Ce L_{III}-edge of $Ce_{1-x}Cu_xO_{2-\delta}$ samples were collected in transmission mode as a function of the temperature using a Si(111) channel-cut monochromator at the LNLS (National Synchrotron Light Laboratory) facility. XANES spectra at Cu K-edge were also acquired. The extraction and fit of the EXAFS spectra were performed using the multi-platform applications for X-ray absorption (MAX) software package[38] and theoretical spectra were obtained using the FEFF9 code.[39] The magnetic measurements were performed in a quantum design superconducting quantum interference device (SQUID) system.

3. Results and discussion

3.1. Electron microscopy and elemental analyses

Fig. 1 presents representative TEM and HRTEM images of the $Ce_{0.95}Cu_{0.05}O_{2-\delta}$ nanoparticles. The samples are composed mainly of nanorods with an average diameter of 10 nm and a length of 70 nm (Fig. 1(a)). The HRTEM images (Fig. 1(b) and (c)) and their respective Fast Fourier Transforms (FFTs) (Fig. 1(d)) confirm the single-crystalline nature of the $Ce_{1-x}Cu_xO_{2-\delta}$ nanostructured samples. The HRTEM results revealed that the growth direction of the nanorods is along the [211] direction. In spite of the few reports on the synthesis of nanorods with the same growth orientation in the literature,[40,41] the growth along the [211] direction has proven to be feasible from the theoretical point of view[42] and is explained by an oriented attachment (OA) process followed by Ostwald ripening of ceria nanocrystals of truncated octahedral shape enclosed by eight {111} and six {200} planes.[41] Using this process the CeO_2 nanocrystals, which act as seeds of the nanorods, may attach by the alignment through the [211] direction leaving exposed the {111} surfaces, or by alignment through the [110] direction with the {200} surfaces exposed. Since the CeO_2{111} surface is the most stable[43,44] the former would be more energetically favorable. These results are in accordance with a previous report,[45] where CeO_2 nanorods were obtained using the same synthesis route. Also, one might say that the introduction of Cu (limited between 1 and 10% Cu in this paper) into the CeO_2 matrix does not affect the morphology of the nanoparticles.

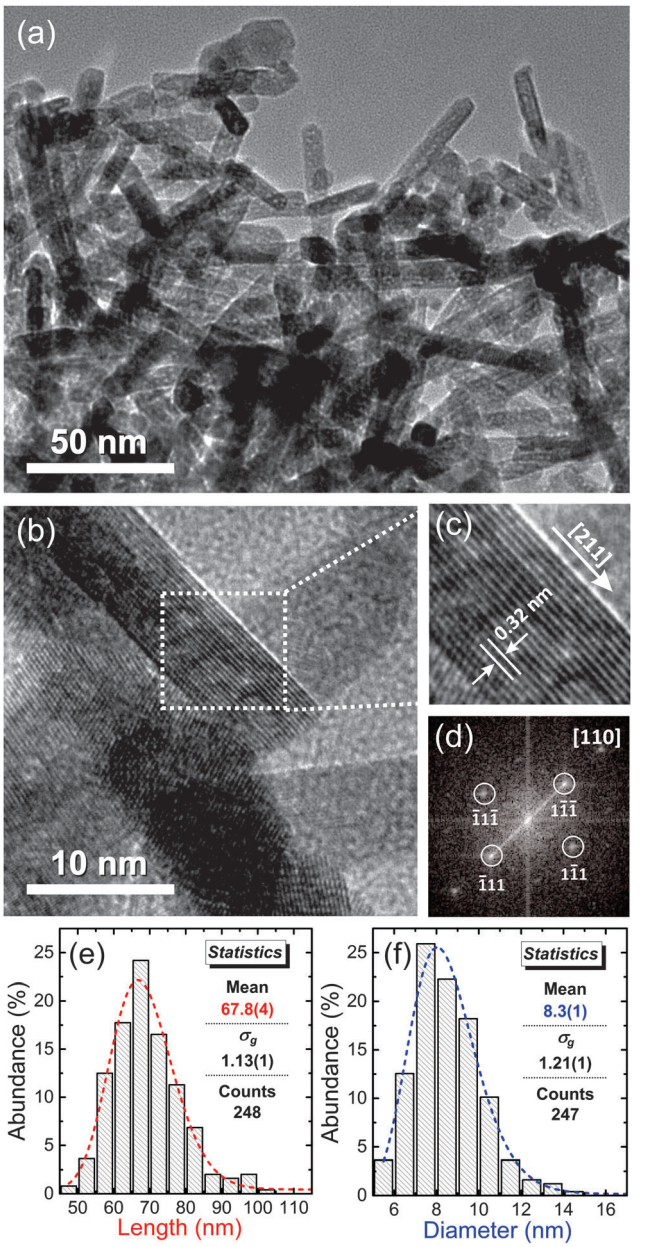

Fig. 1 (a) TEM and (b) HRTEM images of $Ce_{0.95}Cu_{0.05}O_{2-\delta}$ nanorods. (c) Expanded view of the selected region in (b) and (d) Fast Fourier Transform (FFT) of the selected region, zone axis [110]. (e) Length and (f) diameter size distribution histograms. The dashed line in panel (e) and (f) is the log-normal fit.

3.2. X-Ray diffraction

Fig. 2 shows the X-ray diffraction (XRD) patterns for $Ce_{1-x}Cu_xO_{2-\delta}$ nanostructured samples. The typical fluorite CeO_2 structure (ICSD no. 156250) is observed in all samples. CuO peaks were detected only in the sample with 10% of Cu content ($Ce_{0.90}Cu_{0.10}O_{2-\delta}$). No copper or other foreign peaks were observed for the other samples within the XRD detection limit. Table 1 presents the lattice parameter (a) and the oxygen occupancy factor (O_{oc}) calculated from the Rietveld refinement for the whole set of samples. The lattice parameter of our nanostructured undoped CeO_2 sample is slightly bigger than that for bulk CeO_2, 5.411 Å (JCPDS 43-1002). The surface-to-volume fraction is large at the nanoscale, facilitating the oxygen loss from the CeO_2 matrix to an inert gas environment. As mentioned before, these introduced oxygen vacancies lead to the reduction of the oxidation states of the Ce ions (Ce^{4+} into Ce^{3+}),[4] which induces an increase in the lattice parameter due to the decrease in electrostatic forces[46] and due to the bigger ionic radii of Ce^{3+} (ionic radii = 1.283 Å), as compared to the Ce^{4+} (ionic radii = 1.11 Å).[47] The lattice parameters for the Cu-doped samples neither vary with the Cu content nor show significant difference as compared to the undoped one. As pointed out by McBride *et al.*,[48] the resulting lattice constant under doping is not determined solely by the ionic radius. Coulomb effects, oxygen vacancies, and changes in the force constants introduced by doping may also play important roles. In fact, our results are in good agreement with the one obtained by Wang *et al.*,[49] who observed

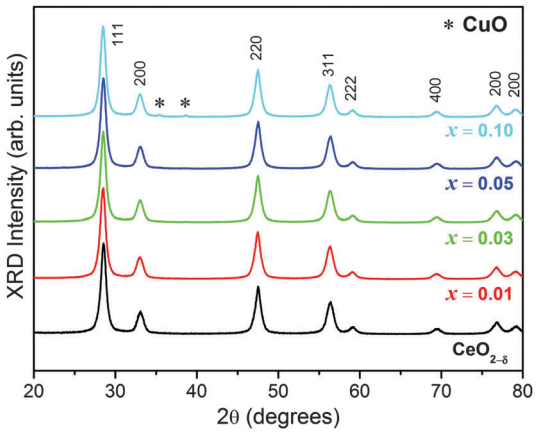

Fig. 2 XRD patterns (CuKα) of $Ce_{1-x}Cu_xO_{2-\delta}$ nanorods.

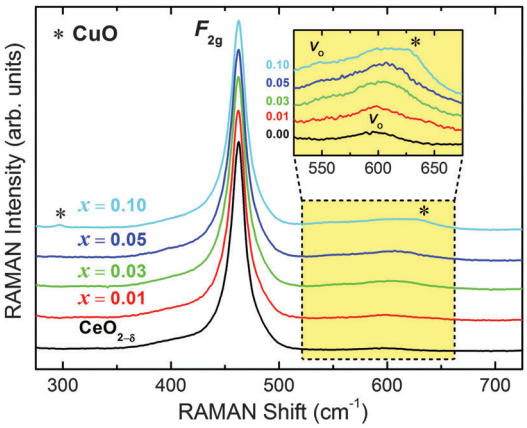

Fig. 3 Raman spectra of the $Ce_{1-x}Cu_xO_{2-\delta}$ nanorods. The inset shows the part of the spectra corresponding to modes associated with oxygen vacancies. The spectra were normalized by the integrated area of the F_{2g} mode. For clarity, the curves are displaced along the vertical axis.

Table 1 Cell parameter (*a*) and occupation factor (O_{oc}) of the $Ce_{1-x}Cu_xO_{2-\delta}$ samples obtained *via* Rietveld refinement

Sample	*a* (Å)	O_{oc}
$CeO_{2-\delta}$	5.417(6)	0.95(4)
$x = 0.01$	5.415(4)	0.96(5)
$x = 0.03$	5.415(3)	0.93(5)
$x = 0.05$	5.415(4)	0.93(6)
$x = 0.10$	5.415(2)	0.89(2)

very small variations in the cell dimension as a consequence of doping ceria with Cu. The small expansion of the $Ce_{1-x}Cu_xO_{2-\delta}$ cell volume was attributed to the O vacancies in the oxide lattice. Wang *et al.*[49] also argue that due to the relatively small size of Cu^{2+} with respect to Ce^{4+},[47] the Cu cations do not fit well in the dodecahedral standard positions for the Ce cations in the ceria lattice and tend to adopt a nearly planar, four-coordinated first shell. In others words, the introduction of O vacancies did not lift the unexpected eight-coordination of the Cu cations and led to a small expansion in the cell dimensions. The expected decrease in oxygen occupancy with increasing copper content is shown in Table 1. The increase of the Ce^{3+} content with copper doping was also further confirmed by analysis of the local structure.

3.3. Raman scattering spectroscopy

Fig. 3 shows the Raman spectra of the samples. Dioxides with a fluorite structure have only one allowed Raman mode, which has a F_{2g} symmetry and can be viewed as a symmetric breathing mode of the oxygen atoms around each cation.[48] Since only the oxygen atoms move, the mode frequency should be nearly independent of the cation mass. In bulk CeO_2 this frequency is 465 cm^{-1}. Here we observed two main features centered at 460 and 600 cm^{-1}. The former is assigned to the fluorite F_{2g} mode, confirming the XRD results. The broad band from 550 to 650 cm^{-1} can be deconvoluted into two main bands, one at 550 cm^{-1} and other at 600 cm^{-1}. The 550 cm^{-1} band is assigned to oxygen vacancies introduced into the ceria in order to maintain charge neutrality when Ce^{4+} ions are replaced with Cu^{2+} ions. Besides, the 600 cm^{-1} band is ascribed to the intrinsic oxygen vacancies due to the presence of Ce^{3+} ions in the ceria matrix, which can be observed in the Raman spectrum for the undoped sample ($CeO_{2-\delta}$).[50] As the copper content increases, the F_{2g} mode shifts slightly to higher frequencies (not shown) and become broader and asymmetric at the low-frequency side, while the mode around 600 cm^{-1} becomes more intense. Since the lattice parameter remains constant with increasing copper content, one can assume that this behavior is due to the increase of oxygen vacancies related to the Cu incorporation into the $CeO_{2-\delta}$ matrix.[48] For the sample with 10% of Cu content ($Ce_{0.90}Cu_{0.10}O_{2-\delta}$), the modes at around 300 and 630 cm^{-1} can be attributed to the CuO segregated phase,[51] corroborating XRD results presented before.

3.4. X-ray absorption

Fig. 4 presents the XANES spectra at Ce L_{III}-edge for $Ce_{1-x}Cu_xO_{2-\delta}$ samples and the spectrum of a CeO_2 standard reference with Ce^{4+}. These spectra result from the configuration interaction due to mixing of Ce 4f and O 2p valence orbitals associated with the crystal-field splitting of the Ce 5d final state.[52] At the pre-edge region the peak denoted as A is associated with a forbidden

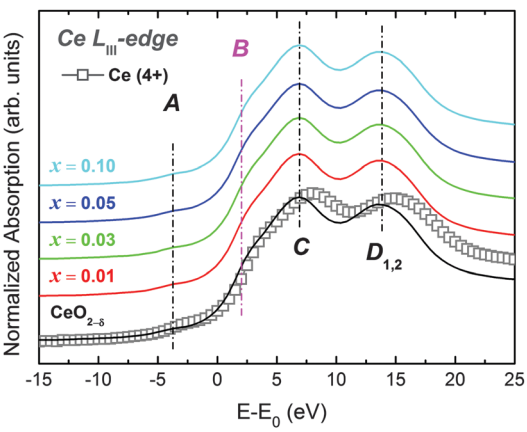

Fig. 4 XANES spectra at Ce L_{III}-edge for $Ce_{1-x}Cu_xO_{2-\delta}$ nanorods.

dipole transition from the bottom of the conduction band.[52] Peaks labeled as C correspond to a transition to the final state of 2p4f $^{1}5d^{1}\underline{v}$ (electron excited from 2p to 5d, with empty 4f; $\underline{v}$ denotes a hole in the valence band) of Ce^{4+}, whereas peaks D_1 and D_2 are also Ce^{4+} peaks, with the final state of 2p4f $^{0}5d^{1}$.[52] As can be seen in Fig. 4, the edge energy for the spectra of $Ce_{1-x}Cu_xO_{2-\delta}$ samples is close to the edge energy of the standard spectrum, indicating a predominance of Ce^{4+}.

The concentration of Ce^{3+} ions in the samples ($[Ce^{3+}]$) can be estimated from the feature labeled as B at the white line of the spectra.[53,54] XANES spectra of all the samples were fitted with Gaussian functions and an arctangent function as the edge jump. The estimated value of $[Ce^{3+}]$ was taken to be the relative intensity of the integrated area of peak B (inset equation in Fig. 5). The results of these analyses are shown in Fig. 5, $[Ce^{3+}]$ being around 7% for the $Ce_{1-x}Cu_xO_{2-\delta}$ samples. In spite of the fitting errors, we can identify an increasing tendency of $[Ce^{3+}]$ as the Cu content increases, a variation of around 1% of the $[Ce^{3+}]$ with the insertion of 10% of Cu into the $CeO_{2-\delta}$ matrix, in good agreement with the calculated and measured variation obtained by Chen *et al.* for Ca^{2+} doped $CeO_{2-\delta}$ samples.[19] As pointed out before, the proportional amount of Ce^{3+} in the CeO_2 system is explained in terms of the Ce^{4+} reduction to Ce^{3+} due to oxygen vacancies.[4] Thereby, this behavior confirms the previous XRD and RAMAN results concerning the introduction of oxygen vacancies into the $CeO_{2-\delta}$ matrix by the Cu-doping due to the charge compensation process and the increase of the Ce^{3+}/Ce^{4+} proportion.

The correlation between the oxygen vacancies and the Cu content in our $CeO_{2-\delta}$ samples was stated by the charge compensation process, the replacement of the Ce ions (Ce^{4+} and Ce^{3+}) by the Cu^{2+} ions. In order to check the 2+ oxidation state of the Cu ions, the XANES spectra at the Cu K-edge were also measured for single phase samples, x = 0.01, 0.03 and 0.05. The valence of the dopant ions can be analyzed and calculated by comparing their resulting edge structures with those obtained from the reference samples.[55] Fig. 6 shows the XANES spectra obtained for our samples and for oxides with different Cu oxidation states,

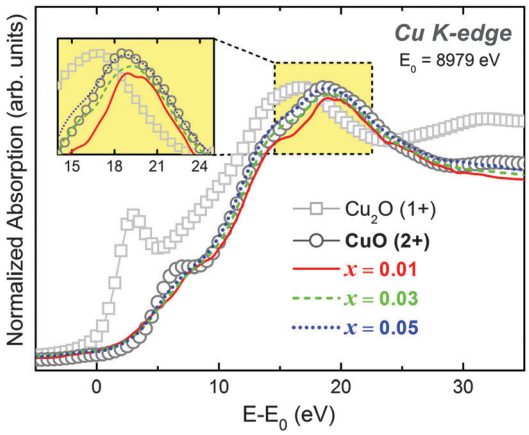

Fig. 6 XANES spectra at Cu K-edge for the single phase Cu doped CeO_2 nanorods (x = 0.01, 0.03 and 0.05). Spectra of Cu_2O (valence 1+), and CuO (valence 2+) are also shown for comparison. The inset highlights the details of the white-line peak.

Cu_2O e CuO. The Cu K-edge spectrum is characterized by a single well-defined peak at the white line which is due to the 1s → 4p electronic transition; the pre-edge peak is due to the dipole-forbidden, quadrupole-allowed 1s → 3d electronic transition and represents a significant feature of Cu^{2+} because there is no 3d vacancy in the Cu^{2+}.[56] The comparison with the spectra from our samples and the calculated oxidation state (+2 ± 0.1) indicates that Cu predominantly assumes the 2+ oxidation state, which corroborates the previous analysis.

The short-range structural data provided by EXAFS offer an element-specific insight, giving quantitative information about the number, position and identity of atoms surrounding the absorbing element as well as structural disorder within the coordination spheres. Fig. 7 shows the modulus of k^3 weighted Fourier transform of single phase $Ce_{1-x}Cu_xO_{2-\delta}$ samples (x = 0, 0.01, 0.03 and 0.05) extracted from Ce L_{III}-edge EXAFS spectra ($\chi(k)$). In order to obtain quantitative information of the local structure around Ce atoms, Fourier transform curves were then back Fourier transformed between 1.5 and 4.5 Å to obtain the

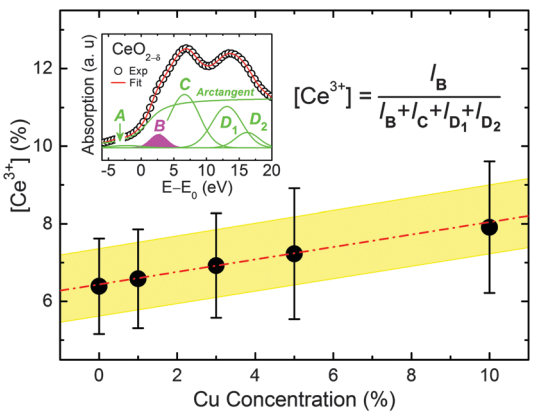

Fig. 5 $[Ce^{3+}]$ concentration calculated from integrated areas (inset equation) obtained by a Gaussian fit of the XANES spectra as a function of Cu concentration. Inset graph presents, as an example, the fitted spectrum for the undoped $CeO_{2-\delta}$.

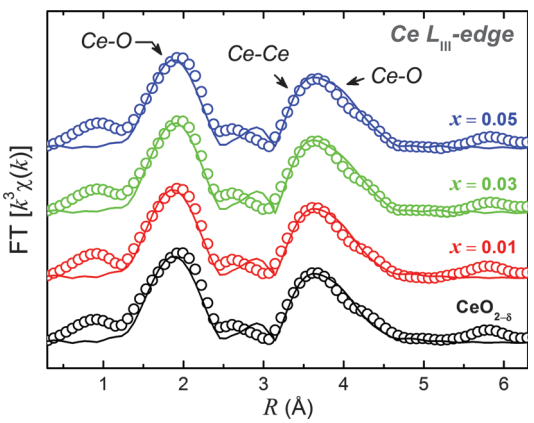

Fig. 7 Experimental and fitted modulus of k^3 weighted Fourier transform for $Ce_{1-x}Cu_xO_{2-\delta}$ nanorods. Open symbols are experimental data, and solid lines represent fittings using the parameters listed in Table 2.

Table 2 Ce L_{III}-edge EXAFS simulation results. R is the distance from the central atom, N is the average coordination number, σ^2 the Debye–Waller factor, and Q the quality factor

Sample	Shell	R (Å)	N	σ^2 ($\times 10^{-3}$ Å^2)	Q
$CeO_{2-\delta}$	Ce–O	2.30(2)	9(1)	12(3)	1.09
	Ce–Ce	3.81(1)	10(1)	5.8(9)	
	Ce–O	4.44(1)	31(6)	15(5)	
$x = 0.01$	Ce–O	2.31(2)	8(1)	11(3)	1.11
	Ce–Ce	3.80(1)	10(1)	5.5(7)	
	Ce–O	4.44(2)	31(7)	17(5)	
$x = 0.03$	Ce–O	2.31(2)	8(1)	10(3)	1.29
	Ce–Ce	3.81(1)	11(2)	6(1)	
	Ce–O	4.45(2)	20(6)	12(6)	
$x = 0.05$	Ce–O	2.30(1)	8(1)	10(3)	1.08
	Ce–Ce	3.81(1)	12(2)	6(1)	
	Ce–O	4.44(2)	20(6)	9(5)	

experimental EXAFS spectra to fit using a theoretical model calculated from the FEFF9 code and crystallographic information according the XRD measurements. In all fits, the number of free parameters was kept smaller than the number of independent points, which is defined as $N_{ind} = 2\Delta R\Delta K/\pi$, where ΔR is the width of the R-space filter windows and ΔK is the actual interval of the fit in the K space.[57] The reliability of the fit, determined by a quality factor (Q),[57] the interatomic distances (R) and Debye–Waller factor (σ^2) relatives to the best fits are shown in Table 2.

According to the structural model, the more intense peak, between 1.5 and 2.5 Å in the Fourier transforms of $Ce_{1-x}Cu_xO_{2-\delta}$ samples, corresponds to a single scattering interaction between the first eight O atoms around the absorber atom. The single scattering interactions relative to Ce–Ce and Ce–O (beyond the first O neighbours) paths correspond the peaks and shoulders observed between 3.0 and 5.0 Å. This region also includes multiple scattering paths such as Ce–O–O, Ce–O–Ce–O, Ce–O–Ce–O, Ce–O–O–O and Ce–Ce–O interactions. It is important to mention that the L_{III}-edge is short in energy, limiting the adjustment and leading to error bars relatively important. The extracted parameters confirm the assumption that Cu doping does not introduce high order disorders into the structure. The radial distance (R) and the coordination number (N) for the first two shells do not change considerably as the Cu content increases. However, we can trace an increase of oxygen vacancies following the average coordination number (N) for the second O-shell. As the Cu content increases the coordination number decreases due to the increase of the oxygen vacancies. The observance of this behavior at the EXAFS data is an indirect evidence that the introduced oxygen vacancies stay close together with the Cu^{2+}.[58,59] It is well known that oxygen vacancies in the interior of $CeO_{2-\delta}$ tend to migrate to the surface.[17,60] However, it is also reasonable to state that the Coulombic attraction energetically favors close proximity between the oxygen vacancies induced by doping and the Cu^{2+} ions forming defect associates (or defect clusters).[4,35,61,62] Recently, experimental and theoretical reports have shown that the oxygen vacancies are attracted to cation dopants that are smaller than the host ions,[63,64] in our case, attracted to Cu^{2+}. These analyses led us to an important conclusion that considering a homogeneous distribution of the Cu^{2+} ions, the introduced oxygen vacancies by the Cu-doping are pinned along the volume of the $CeO_{2-\delta}$ nanorods, avoiding any aging process due to oxidation at the surfaces of the nanorods. The homogeneous distribution of the Cu^{2+} ions over the volume of the samples was further confirmed by magnetic analyses.

3.5. Magnetic characterization

The measurements of the magnetic moment (M) as a function of magnetic field (H) are presented in Fig. 8. The sample holder magnetic contribution to the raw data was carefully subtracted following standard procedures. For the undoped $CuO_{2-\delta}$ sample the results at 300 K (Fig. 8(a)) show a typical diamagnetic behavior; however, at 2 K (Fig. 8(b)) the obtained $M(H)$ curve also reveals a relatively small paramagnetic component. The diamagnetic phase of the undoped $CuO_{2-\delta}$ matrix is associated with the Ce^{4+} ions, while the paramagnetic component comes from the Ce^{3+} ions.[65] Considering that the concentration of the Ce^{3+} ions in the samples is almost constant (Fig. 5), the magnetic properties associated solely with the Cu^{2+} ions can be obtained by subtracting the diamagnetic (Ce^{4+}) and the paramagnetic (Ce^{3+}) backgrounds determined by the measurements of the undoped $CeO_{2-\delta}$ sample. Fig. 8(a) and 8(b) also present the obtained $M(H)$ curves for the Cu-doped samples after subtract the $CeO_{2-\delta}$ matrix magnetic components. All Cu-doped samples present only paramagnetic behavior. It is

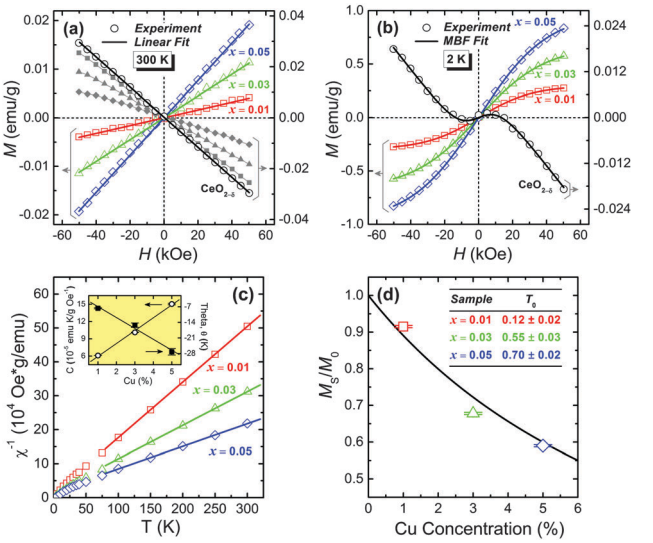

Fig. 8 $M(H)$ curves of the undoped $CeO_{2-\delta}$ and of the single phase $Ce_{1-x}Cu_xO_{2-\delta}$ nanorods (x = 0.01, 0.03 and 0.05) at (a) 300 and at (b) 2 K. Symbols are the experimental data, and lines are fits using a Modified Brillouin Function (MBF). The gray small full symbols in (a) correspond to the raw data obtained for the Cu-doped samples before the subtraction of the $CeO_{2-\delta}$ matrix contribution. (c) dc magnetic susceptibility as a function of temperature for the single phase $Ce_{1-x}Cu_xO_{2-\delta}$ nanorods. The best fit of the Curie–Weiss law is shown as solid lines. The inset shows C and θ a function of the Cu content; solid lines are linear fit to the data. (d) Ratio M_S/M_0 (also called $\bar{x}/x$) as a function of Cu content. The solid line represents the theoretical value expected for a random distribution of the Cu ions in a fcc structure. The inset table shows the T_0 parameter obtained by the MBF fitting.

important to stress that any evidence of a ferromagnetic phase could be observed, even for the undoped $CeO_{2-\delta}$ sample. Fig. 8(b) shows that the saturation magnetization from the paramagnetic response of the Ce^{3+} in the $CeO_{2-\delta}$ matrix is at least 20-fold smaller than in the Cu-doped samples. The large difference observed validates the procedure of subtraction of the $CeO_{2-\delta}$ response from the Cu-doped ones even though the paramagnetic component is associated with the Ce^{3+} ions in the former.

The inverse of the dc magnetic susceptibility as a function of temperature is presented in Fig. 8(c). We shall analyze this result according to the discussion of Spalek *et al.*[66] The inverse of the susceptibility were fitted in the range of high temperature using the Curie–Weiss Law: $\chi(T) = C/(T - \theta)$; where C is the Curie constant per gram and θ is the Curie–Weiss temperature per gram. C and θ are both linear functions of the Cu content x: $C = xC_0$ and $\theta = x\theta_0$, where $C_0 = N(g\mu_B)^2S(S + 1)/3k_B$ and $\theta_0 = 2zS(S + 1)J_1/3k_B$. Here, N is the total number of cations per gram, g the effective Landé factor of the Cu ions, we assumed $J = S = 1/2$, μ_B is the Bohr magneton, z is the number of nearest-neighbor cations ($z = 12$ in the fluorite structure), J_1 is the effective exchange integral constant, and k_B is the Boltzmann constant. From our data we obtain the two main magnetic parameters for Cu^{2+}: $g = 2.0 \pm 0.1$ and $J_1 = -57 \pm 7$ cm^{-1}. These values are in good agreement with the experimental data found in the literature.[67,68] The negative value for J_1 indicates an antiferromagnetic coupling between the Cu^{2+} ions. Below 100 K, the inverse susceptibility deviates from the linear dependence, the Curie–Weiss law, toward zero. This feature is due to additional antiferromagnetic interactions related to distant neighbors, which become considerably large at values of low temperature.[66] This feature is also observed for different DMOs.[14,69,70]

The low temperature $M(H)$ curves (Fig. 8(b)) are also consistent with the existence of antiferromagnetic coupling between Cu^{2+} ion moments. These data were fitted by a Modified Brillouin Function (MBF) expressed as $M = M_S B_{1/2}(g\mu_B H/2k_B(T + T_0))$;[71,72] where $B_{1/2}$ is the Brillouin function for spin $S = 1/2$, but with a temperature replaced by an effective temperature $T + T_0$ (T_0 corresponds to a correction term of the measurement temperature T and it is due to distant neighbor interactions) and M_S is the technical saturation magnetization, not the theoretical saturation magnetization M_0. We have assumed $g = 2$ and $S = 1/2$ for the Cu^{2+} ions from the susceptibility results. The two main parameters extracted from the MBF fitting for the samples, the M_S/M_0 ratio and the correction term of the temperature, T_0, are presented in Fig. 8(d). The line represents the theoretical M_S/M_0 ratio calculated for a cluster model considering a random distribution of the magnetic dopants (Cu^{2+}) over a fcc matrix structure (CeO_2 fluorite structure) with antiferromagnetic exchange interaction only between the first neighbors.[73] The good agreement observed between the obtained experimental M_S/M_0 ratio and the theoretical curve in Fig. 8(d) is a strong evidence for a random distribution of the Cu^{2+} ions in the studied samples with an antiferromagnetic coupling between them. The random distribution of the Cu^{2+} ions over the volume of the samples confirms the previous assumption related to their homogeneous distribution. We also extract from the MBF fitting of $M(H)$ curves, positive T_0 values for all the samples; we also observe that T_0 values increase as Cu^{2+} contents increase (inset table in Fig. 8(d)). These results are quite in line with other reports for different DMOs,[74,75] and reflect that the distant-neighbor antiferromagnetic interactions have considerable magnitude as compared to the temperature of the measurements (2 K) and are directly proportional to the doping amount.[72]

As mentioned before, the main papers concerning the origin of ferromagnetism in $CeO_{2-\delta}$ nanoparticles assume that it may be associated with oxygen[3,9,19] or cerium[9,22] vacancies, both located at the surfaces of the nanoparticles. The cerium vacancies must be ruled out for the $CeO_{2-\delta}$ system, since under the equilibrium conditions its formation energy is relatively high as compared to the formation energy of other defects.[76] Considering the oxygen vacancies under the scope of the FCE theory, Chen *et al.*[19] explained the observed RTFM by the formation of magnetic centers composed of oxygen vacancies and trapped electrons donated by adsorbed elements on the surface/interfaces of the nanoparticles. Moreover, Ge *et al.*[20] verified that $CeO_{2-\delta}$ nanocubes exhibit stronger ferromagnetic behavior than $CeO_{2-\delta}$ nanoparticles.[20] They presented first-principles calculations of oxygen vacancies sites in {100} $CeO_{2-\delta}$ surfaces and bulk, showing that the magnetic moment associated with the oxygen vacancies is higher when the oxygen vacancies are located at the {100} surface. However, their calculated bulk magnetic moment is still significant, 1.41 μ_B for the bulk compared to 1.98 μ_B for the {100} surface.

Although according to our structural analysis, all of our samples presented oxygen vacancies, whose number increases with the inclusion of Cu^{2+} ions, our undoped sample reveals to be diamagnetic while the single phase Cu-doped samples present only a paramagnetic behavior. Remembering that the introduced oxygen vacancies are mainly distributed in the bulk of the samples, we can state that, contrary to Ge *et al.*,[20] oxygen vacancies on the bulk of the $CeO_{2-\delta}$ matrix cannot be responsible for the reported RTFM in the literature. Nevertheless, we would also expect oxygen vacancies at the surfaces of the nanorods due to oxygen losses to the environment that would lead to an observation of a RTFM, once we conclude that oxygen vacancies and defects at the surfaces dominate the mechanism for the RTFM. Here we have to take into consideration that our nanorods were grown in the [211] direction by an attachment process of ceria nanocrystals of truncated octahedron shape enclosed by eight {111} and six {200} planes, leaving exposed the {111} surfaces. In the literature a morphology-dependent phenomenon closely related to the nature of the exposed crystal planes and crystalline structure in $CeO_{2-\delta}$ systems has been reported,[77,78] and it has to be considered. Between the three low-index planes in the fluorite cube structure, ({111}, {110} and {001}), the {111} surface is the most stable and neutral.[44] The energy required to create oxygen vacancies on the surfaces is related to their stabilities, and since the {111} surface is the most stable one, it is, thus, less reactive than the other surfaces.[43,79,80] Therefore the {111} surfaces will only present a relative small proportion of oxygen vacancies and adsorbed elements, which would provide the necessary electrons to form a magnetic polaron, considering the proposed model by Chen *et al.*[19] Thus, only isolated single or small clusters of magnetic polarons may be considered on the {111} surfaces, which would not lead to

the establishment of a long range magnetic ordering in the studied nanorods, or even in the truncated octahedral nanocrystals seeds, since their exposed surfaces are predominantly composed of {111} surfaces.[81] All these analyses lead us to conclude the association with the RTFM to oxygen vacancies exclusively located at the surface of $CeO_{2-\delta}$ nanoparticles.

4. Conclusions

The microwave-assisted hydrothermal method is an efficient method for the synthesis of $Ce_{1-x}Cu_xO_{2-\delta}$ with up to 5% of Cu content. HRTEM shows nanorods with a size of 10 nm in diameter and 70 nm in length and a single cubic $CeO_{2-\delta}$ phase with an exposed {111} crystallographic plane. The structural analysis shows that Cu^{2+} doping does not change the $CeO_{2-\delta}$ cubic structure, but the inclusion of Cu^{2+} leads to the increase of O vacancies in the system. The XANES spectra also reveal that the incorporation of Cu^{2+} in the $CeO_{2-\delta}$ matrix leads to an increase of $[Ce^{3+}]$, also contributing to the increase of O vacancies. From the EXAFS results we could state that the O vacancies introduced by the Cu doping are located close to the Cu^{2+} ions in the bulk of the nanorods. The magnetic characterization reveals a diamagnetic phase associated with a paramagnetic phase for the undoped sample and only a paramagnetic behavior for the Cu-doped samples, contrary to some reports. Any ferromagnetic phase could be observed. This leads us to conclude that the presence of oxygen vacancies is not a sufficient condition to mediate ferromagnetic order in $CeO_{2-\delta}$ samples, since their location site on the structure also plays a vital role.

Acknowledgements

Support from the agencies FAPEMIG, CNPq, CAPES (PNPD-2011), FINEP, MINECO (MAT2012-33483) and FAPESP is gratefully acknowledged. We also thank CNPq and CAPES for research fellowships (ACD, AOZ and AM). The authors also acknowledge LNLS for the XAS measurements and Prof. Dr F. Iikawa and Prof. Dr M. J. S. Brasil of the Universidade de Campinas (UNICAMP) for the Raman measurements.

Notes and references

1 Y. Y. Li, X. Dong, J. S. Gao, D. Q. Hei, X. C. Zhou and H. Q. Zhang, *Physica E*, 2009, **41**, 1550.
2 A. Tiwari, V. M. Bhosle, S. Ramachandran, N. Sudhakar, J. Narayan, S. Budak and A. Gupta, *Appl. Phys. Lett.*, 2006, **88**, 142511.
3 A. Sundaresan, R. Bhargavi, N. Rangarajan, U. Siddesh and C. N. R. Rao, *Phys. Rev. B: Condens. Matter Mater. Phys.*, 2006, **74**, 161306.
4 M. Mogensen, N. M. Sammes and G. A. Tompsett, *Solid State Ionics*, 2000, **129**, 63.
5 J. M. D. Coey, K. Wongsaprom, J. Alaria and M. Venkatesan, *J. Phys. D: Appl. Phys.*, 2008, **41**, 134012.
6 J. M. D. Coey, M. Venkatesan and C. B. Fitzgerald, *Nat. Mater.*, 2005, **4**, 173.
7 M. J. Calderon and S. D. Sarma, *Ann. Phys.*, 2007, **322**, 2618.
8 J. M. D. Coey, A. P. Douvalis, C. B. Fitzgerald and M. Venkatesan, *Appl. Phys. Lett.*, 2004, **84**, 1332.
9 V. Fernandes, R. J. O. Mossanek, P. Schio, J. J. Klein, A. J. A. de Oliveira, W. A. Ortiz, N. Mattoso, J. Varalda, W. H. Schreiner, M. Abbate and D. H. Mosca, *Phys. Rev. B: Condens. Matter Mater. Phys.*, 2009, **80**, 035202.
10 A. K. Rumaiz, B. Ali, A. Ceylan, M. Boggs, T. Beebe and S. I. Shah, *Solid State Commun.*, 2007, **144**, 334.
11 N. H. Hong, J. Sakai, N. Poirot and V. Brize, *Phys. Rev. B: Condens. Matter Mater. Phys.*, 2006, **73**, 132404.
12 J. B. Yi, C. C. Lim, G. Z. Xing, H. M. Fan, L. H. Van, S. L. Huang, K. S. Yang, X. L. Huang, X. B. Qin, B. Y. Wang, T. Wu, L. Wang, H. T. Zhang, X. Y. Gao, T. Liu, A. T. S. Wee, Y. P. Feng and J. Ding, *Phys. Rev. Lett.*, 2010, **104**, 137201.
13 L. R. Shah, W. G. Wang, H. Zhu, B. Ali, Y. Q. Song, H. W. Zhang, S. I. Shah and J. Q. Xiao, *J. Appl. Physiol.*, 2009, **105**, 07C515.
14 T. E. de Souza, A. Mesquita, A. O. de Zevallos, F. Beron, K. R. Pirota, P. P. Neves, A. C. Doriguetto and H. B. de Carvalho, *J. Phys. Chem. C*, 2013, **117**, 13252.
15 M. P. F. de Godoy, A. Mesquita, W. Avansi, P. P. Neves, V. A. Chitta, W. B. Ferraz, M. A. Boselli, A. C. S. Sabioni and H. B. de Carvalho, *J. Alloys Compd.*, 2013, **555**, 315.
16 S. Tsunekawa, R. Sivamohan, S. Ito, A. Kasuya and T. Fukuda, *Nanostruct. Mater.*, 1999, **11**, 141.
17 L. J. Wu, H. J. Wiesmann, A. R. Moodenbaugh, R. F. Klie, Y. M. Zhu, D. O. Welch and M. Suenaga, *Phys. Rev. B: Condens. Matter Mater. Phys.*, 2004, **69**, 125415.
18 S. Y. Chen, Y. H. Lu, T. W. Huang, D. C. Yan and C. L. Dong, *J. Phys. Chem. C*, 2010, **114**, 19576.
19 X. B. Chen, G. S. Li, Y. G. Su, X. Q. Qiu, L. P. Li and Z. G. Zou, *Nanotechnology*, 2009, **20**, 115606.
20 M. Y. Ge, H. Wang, E. Z. Liu, J. F. Liu, J. Z. Jiang, Y. K. Li, Z. A. Xu and H. Y. Li, *Appl. Phys. Lett.*, 2008, **93**, 062505.
21 X. P. Han, J. Lee and H. I. Yoo, *Phys. Rev. B: Condens. Matter Mater. Phys.*, 2009, **79**, 100403.
22 Y. L. Liu, Z. Lockman, A. Aziz and J. MacManus-Driscoll, *J. Phys.: Condens. Matter*, 2008, **20**, 165201.
23 M. J. Li, S. H. Ge, W. Qiao, L. Zhang, Y. L. Zuo and S. M. Yan, *Appl. Phys. Lett.*, 2009, **94**, 152511.
24 S. Komarneni, *Curr. Sci.*, 2003, **85**, 1730.
25 G. Avgouropoulos, T. Ioannides, C. Papadopoulou, J. Batista, S. Hocevar and H. Matralis, *Catal. Today*, 2002, **75**, 157.
26 J. Beckers and G. Rothenberg, *Dalton Trans.*, 2008, 6573.
27 P. Djinovic, J. Batista, J. Levec and A. Pintar, *Appl. Catal., A*, 2009, **364**, 156.
28 D. L. Hou, H. J. Meng, L. Y. Jia, X. J. Ye, H. J. Zhou and X. L. Li, *EPL*, 2007, **78**, 67001.
29 E. Wiberg, A. F. Holleman and N. Wiberg, *Inorganic chemistry*, Academic Press, San Diego, Berlin, New York, 2001.
30 M. W. Barsoum, *Fundamentals of ceramics*, Taylor & Francis, New York, London, 2003.
31 M. Nolan, *J. Mater. Chem.*, 2011, **21**, 9160.
32 S. Y. Chen, K. W. Fong, T. T. Peng, C. L. Dong, A. Gloter, D. C. Yan, C. L. Chen, H. J. Lin and C. T. Chen, *J. Phys. Chem. C*, 2012, **116**, 26570.

33 P. Slusser, D. Kumar and A. Tiwari, *Appl. Phys. Lett.*, 2010, **96**, 142506.
34 M. S. Seehra, S. Suri and V. Singh, *J. Appl. Physiol.*, 2012, **111**, 07B516.
35 F. Li, C. W. Zhang and M. W. Zhao, *J. Appl. Physiol.*, 2012, **112**, 083702.
36 V. Fernandes, P. Schio, A. J. A. de Oliveira, W. H. Schreiner, J. Varalda and D. H. Mosca, *J. Appl. Physiol.*, 2011, **110**, 113902.
37 A. C. Larson and R. B. V. Dreele, General Structure Analysis System (GSAS), Los Alamos National Laboratory Report LAUR 86-7481994.
38 A. Michalowicz, J. Moscovici, D. Muller-Bouvet and K. Provost, *J. Phys.: Conf. Ser.*, 2009, **190**, 012034.
39 A. L. Ankudinov, B. Ravel, S. D. Conradson and J. J. Rehr, *Phys. Rev. B: Condens. Matter Mater. Phys.*, 1998, **58**, 7565.
40 Z. Ji, X. Wang, H. Zhang, S. Lin, H. Meng, B. Sun, S. George, T. Xia, A. E. Nel and J. I. Zink, *ACS Nano*, 2012, **6**, 5366.
41 N. Du, H. Zhang, B. G. Chen, X. Y. Ma and D. R. Yang, *J. Phys. Chem. C*, 2007, **111**, 12677.
42 T. X. T. Sayle, B. J. Inkson, A. Karakoti, A. Kumar, M. Molinari, G. Mobus, S. C. Parker, S. Seal and D. C. Sayle, *Nanoscale*, 2011, **3**, 1823.
43 D. C. Sayle, S. A. Maicaneanu and G. W. Watson, *J. Am. Ceram. Soc.*, 2002, **124**, 11429.
44 F. Zhang, Q. Jin and S. W. Chan, *J. Appl. Physiol.*, 2004, **95**, 4319.
45 V. D. Araujo, W. Avansi, H. B. de Carvalho, M. L. Moreira, E. Longo, C. Ribeiro and M. I. B. Bernardi, *CrystEngComm*, 2012, **14**, 1150.
46 S. Tsunekawa, K. Ishikawa, Z. Q. Li, Y. Kawazoe and A. Kasuya, *Phys. Rev. Lett.*, 2000, **85**, 3440.
47 R. Shannon, *Acta Crystallogr., Sect. A: Cryst. Phys., Diffr., Theor. Gen. Crystallogr.*, 1976, **32**, 751.
48 J. R. Mcbride, K. C. Hass, B. D. Poindexter and W. H. Weber, *J. Appl. Physiol.*, 1994, **76**, 2435.
49 X. Q. Wang, J. A. Rodriguez, J. C. Hanson, D. Gamarra, A. Martinez-Arias and M. Fernandez-Garcia, *J. Phys. Chem. B*, 2005, **109**, 19595.
50 Z. D. Dohcevic-Mitrovic, M. Grujic-Brojcin, M. Scepanovic, Z. V. Popovic, S. Boskovic, B. Matovic, M. Zinkevich and F. Aldinger, *J. Phys.: Condens. Matter*, 2006, **18**, S2061.
51 J. Chrzanowski and J. C. Irwin, *Solid State Commun.*, 1989, **70**, 11.
52 V. Fernandes, P. Schio, A. J. A. de Oliveira, W. A. Ortiz, P. Fichtner, L. Amaral, I. L. Graff, J. Varalda, N. Mattoso, W. H. Schreiner and D. H. Mosca, *J. Phys.: Condens. Matter*, 2010, **22**, 216004.
53 P. Nachimuthu, W. C. Shih, R. S. Liu, L. Y. Jang and J. M. Chen, *J. Solid State Chem.*, 2000, **149**, 408.
54 A. M. Shahin, F. Grandjean, G. J. Long and T. P. Schuman, *Chem. Mater.*, 2005, **17**, 315.
55 T. Vitova, J. Hormes, K. Peithmann and T. Woike, *Phys. Rev. B: Condens. Matter Mater. Phys.*, 2008, **77**, 144103.
56 A. Al-Ebraheem, J. Goettlicher, K. Geraki, S. Ralph and M. J. Farquharson, *X-Ray Spectrom.*, 2010, **39**, 332.
57 S. S. Hasnain, Report on the International Workshops on Standards and Criteria in XAFS. X-ray Absorption Fine Structure: Proceedings of the VI International Conference on X-ray Absorption Fine Structures, Ellis Horwood New York, 1991.
58 T. Ohashi, S. Yamazaki, T. Tokunaga, Y. Arita, T. Matsui, T. Harami and K. Kobayashi, *Solid State Ionics*, 1998, **113**, 559.
59 P. Bera, K. R. Priolkar, P. R. Sarode, M. S. Hegde, S. Emura, R. Kumashiro and N. P. Lalla, *Chem. Mater.*, 2002, **14**, 3591.
60 J. C. Conesa, *Surf. Sci.*, 1995, **339**, 337.
61 N. V. Skorodumova, S. I. Simak, B. I. Lundqvist, I. A. Abrikosov and B. Johansson, *Phys. Rev. Lett.*, 2002, **89**, 166601.
62 K. Q. Huang, M. Feng and J. B. Goodenough, *J. Am. Ceram. Soc.*, 1998, **81**, 357.
63 S. Sen, H. J. Avila-Paredes and S. Kim, *J. Mater. Chem.*, 2008, **18**, 3915.
64 X. Wei, W. Pan, L. F. Cheng and B. Li, *Solid State Ionics*, 2009, **180**, 13.
65 P. Dutta, S. Pal, M. S. Seehra, Y. Shi, E. M. Eyring and R. D. Ernst, *Chem. Mater.*, 2006, **18**, 5144.
66 J. Spalek, A. Lewicki, Z. Tarnawski, J. K. Furdyna, R. R. Galazka and Z. Obuszko, *Phys. Rev. B: Condens. Matter Mater. Phys.*, 1986, **33**, 3407.
67 C. Kittel, *Introduction to solid state physics*, Wiley, New York, Chichester, 1996.
68 M. Che and J. C. Védrine, *Characterization of solid materials and heterogeneous catalysts: from structure to surface reactivity*, Wiley-VCH, Weinheim, 2012.
69 S. Kolesnik, B. Dabrowski and J. Mais, *J. Appl. Physiol.*, 2004, **95**, 2582.
70 H. Alawadhi, I. Miotkowski, A. Lewicki, A. K. Ramdas, S. Miotkowska and M. McElfresh, *J. Phys.: Condens. Matter*, 2002, **14**, 4611.
71 D. Heiman, Y. Shapira, S. Foner, B. Khazai, R. Kershaw, K. Dwight and A. Wold, *Phys. Rev. B: Condens. Matter Mater. Phys.*, 1984, **29**, 5634.
72 J. A. Gaj, R. Planel and G. Fishman, *Solid State Commun.*, 1979, **29**, 435.
73 Y. Shapira, S. Foner, D. H. Ridgley, K. Dwight and A. Wold, *Phys. Rev. B: Condens. Matter Mater. Phys.*, 1984, **30**, 4021.
74 P. Sati, C. Deparis, C. Morhain, S. Schafer and A. Stepanov, *Phys. Rev. Lett.*, 2007, **98**, 137204.
75 C. J. M. Denissen, H. Nishihara, J. C. Vangool and W. J. M. Dejonge, *Phys. Rev. B: Condens. Matter Mater. Phys.*, 1986, **33**, 7637.
76 P. R. L. Keating, D. O. Scanlon, B. J. Morgan, N. M. Galea and G. W. Watson, *J. Phys. Chem. C*, 2012, **116**, 2443.
77 T. M. Zhang, J. Li, H. Li, Y. Li and W. Shen, *Catal. Today*, 2009, **148**, 179.
78 R. Si and M. Flytzani-Stephanopoulos, *Angew. Chem., Int. Ed.*, 2008, **47**, 2884.
79 B. Skarman, T. Nakayama, D. Grandjean, R. E. Benfield, E. Olsson, K. Niihara and L. R. Wallenberg, *Chem. Mater.*, 2002, **14**, 3686.
80 M. Lundberg, B. Skarman and L. R. Wallenberg, *Microporous Mesoporous Mater.*, 2004, **69**, 187.
81 K. Zhou, X. Wang, X. Sun, Q. Peng and Y. Li, *J. Catal.*, 2005, **229**, 206.

